NANO LETTERS

pubs.acs.org/NanoLett Letter

Soliton-Dependent Electronic Transport across Bilayer Graphene Domain Wall

Lili Jiang,[‖] Sheng Wang,[‖] Sihan Zhao, Michael Crommie, and Feng Wang*

Cite This: *Nano Lett.* 2020, 20, 5936−5942 Read Online

ACCESS | Metrics & More | Article Recommendations | Supporting Information

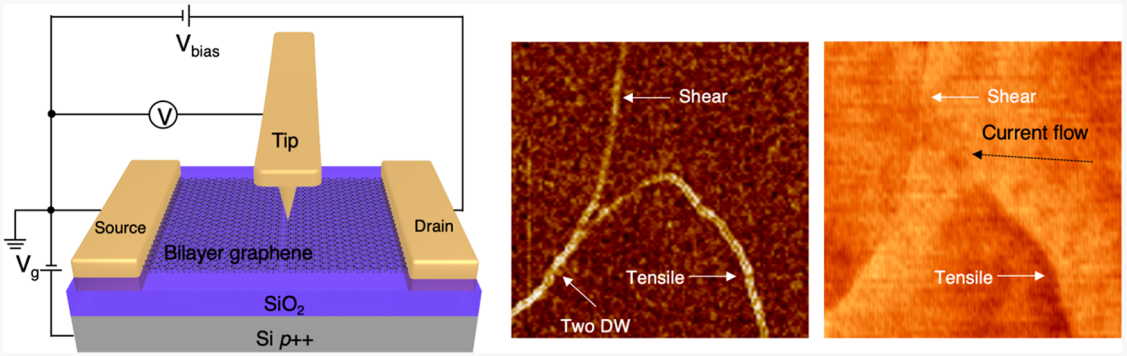

ABSTRACT: Layer-stacking domain wall in bilayer graphene is one type of topological defects that can greatly affect the electronic properties of bilayer graphene and therefore lead to nontrivial transport behaviors. An outstanding question on the layer stacking domain wall is how the electrons hop between two adjacent stacking domains. Here we report the first experimental observation of electronic transport across bilayer graphene domain walls by combining near-field infrared nanoscopy and scanning voltage microscopy techniques. We observe markedly different electron transport behaviors across the tensile- and shear-type domain walls. The tensile-type domain wall is highly reflective of low-energy incident electrons, but becomes more transparent when the electron density and the Fermi energy are increased by electrostatic gating. In contrast, the shear-type domain wall is always highly transparent at different gate voltages. Such soliton-dependent electronic transport can open up new routes to engineer novel nanoelectronic devices based on layer-stacking domain walls in bilayer graphene.

KEYWORDS: *Bilayer graphene, Layer-stacking domain walls, Scanning voltage microscope, Topological defects*

INTRODUCTION

Layer-stacking domain walls in bilayer graphene are one-dimensional solitons that exhibit distinctive electrical,[1−10] optical,[11,12] and mechanical[13−16] properties. For example, transport along the domain walls has been shown to feature topologically protected quantum valley Hall edge states, which provides the ways to control the valley degree of freedom for valleytronic devices. In addition, twisted bilayer graphene, which can be viewed as a domain wall network of AB/BA graphene domains, has been shown to exhibit novel electrical transport behavior. They are formed between AB and BA domains, where one of the graphene layers moves with respect to the other by a single carbon−carbon bond along the armchair directions.[11,13,17] Periodic lattices of layer stacking domains in twisted atomically thin crystals, such as AB and BA stacking domains in twisted bilayer graphene, give rise to a moiré superlattice that can dramatically modify their electrical[18−27] and optical[12] properties. Detailed study of the coupling between adjacent stacking domains across the layer stacking domain wall is of critical importance for quantitative understanding of the various emerging domain wall physics in different bilayer graphene systems.

Different types of domain wall can form based on its crystallographic orientation and the Burgers vector, which represents the magnitude and direction of the lattice distortion in crystals. Two limiting cases are tensile- and shear-type domain walls: the orientation of a tensile-type domain wall (Figure 1a) is perpendicular to its Burgers vector, and the orientation of a shear-type domain wall (Figure 1b) is along its Burgers vector. Distinct electrical and optical properties can exist at different types of domain wall solitons. For example, the reflection of the two-dimensional plasmons at a bilayer graphene domain wall has been found to be soliton-

Received: May 2, 2020
Revised: June 24, 2020
Published: June 26, 2020

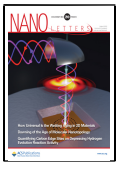

https://dx.doi.org/10.1021/acs.nanolett.0c01911
Nano Lett. 2020, 20, 5936−5942

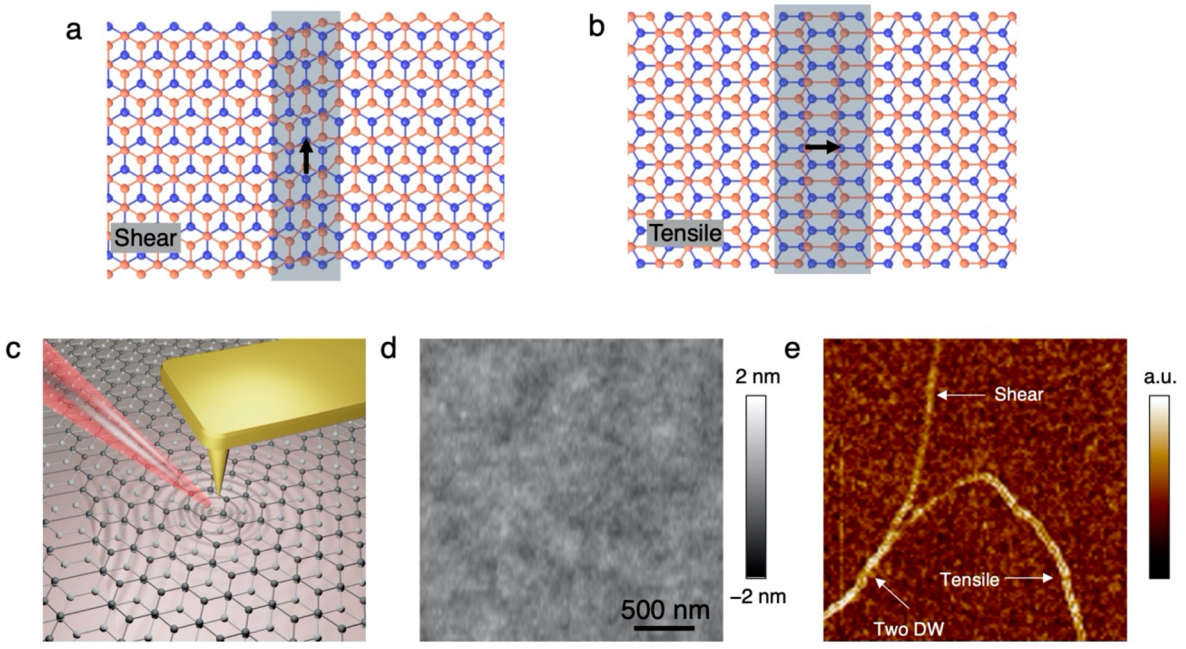

Figure 1. Infrared nanoimaging of domain wall solitons in bilayer graphene. (a,b) The schematics of shear (a) and tensile (b) domain walls in bilayer graphene. The black arrows represent the Burgers Vector of the domain wall solitons. The shear type domain wall is parallel with its Burgers Vector, while the tensile domain wall is perpendicular to its Burgers Vector. (c) The schematic of the infrared nanoscopy technique used to identify different types of domain walls in bilayer graphene. (d) AFM topography image of a bilayer graphene flake on SiO_2/Si substrate, which is almost featureless. (e) The corresponding near-field infrared image taken simultaneously with the topography image. The obvious bright lines in the near-field image are layer-stacking domain walls. In the near-field image, the shear domain wall exhibits a single-line feature (upper segment) and the tensile domain wall exhibits a double-line feature (lower-left segment).

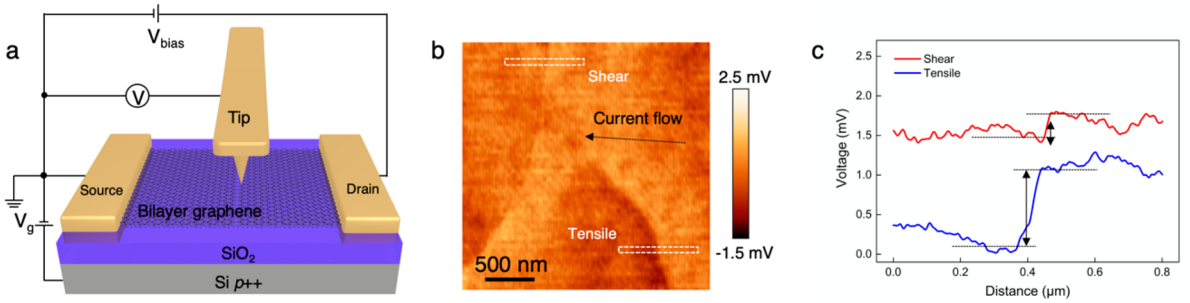

Figure 2. Imaging the voltage drops across single domain walls. (a) Schematic of the scanning voltage microscopy technique used to map the potential distribution of bilayer graphene transistors. (b) Voltage map of the same area as in Figure 1d,e. The average current flow is along the dashed arrow. (c) Line profiles of the voltage across the shear (red line) and the tensile (blue) domain walls which are shown in (b) (averaged in white dashed areas to increase the signal-to-noise ratio). The magnitude of the extra voltage drop at the tensile domain wall is stronger than that at the shear domain wall.

dependent.[11] The anisotropic movement of the domain wall by mechanical force is also determined by their types.[14] Electron transmission across the domain wall, which determines the electrical coupling between adjacent layer-stacking domains, is also expected to be strongly soliton-type dependent.[28] However, the experimental study of the electronic transport across the extremely narrow domain wall has been challenging because the bulk graphene transport can easily dominate over the domain wall contribution to the resistivity in a typical graphene device. It is even harder to distinguish the contribution from different types of domain walls by the conventional transport measurement.

In this Letter, we report the soliton-dependent electronic transport across the stacking domain walls in bilayer graphene. We first identify different types of domain wall solitons using near-field infrared nanoscopy. Then we obtain real-space image of the electronic transport through individual domain walls using scanning voltage microscopy (SVM), which can extract the local voltage drop induced by the domain walls. Our study reveals distinctive transport behaviors across the tensile- and shear-type domain walls. The tensile domain walls exhibit much lower transparency compared to the shear domain walls. The tensile domain walls show highly reflective feature at low doping and the carrier transmission will monotonically increase with increasing carrier density. In contrast, the shear domain walls remain highly transparent at a large range of gate voltages.

https://dx.doi.org/10.1021/acs.nanolett.0c01911
Nano Lett. 2020, 20, 5936−5942

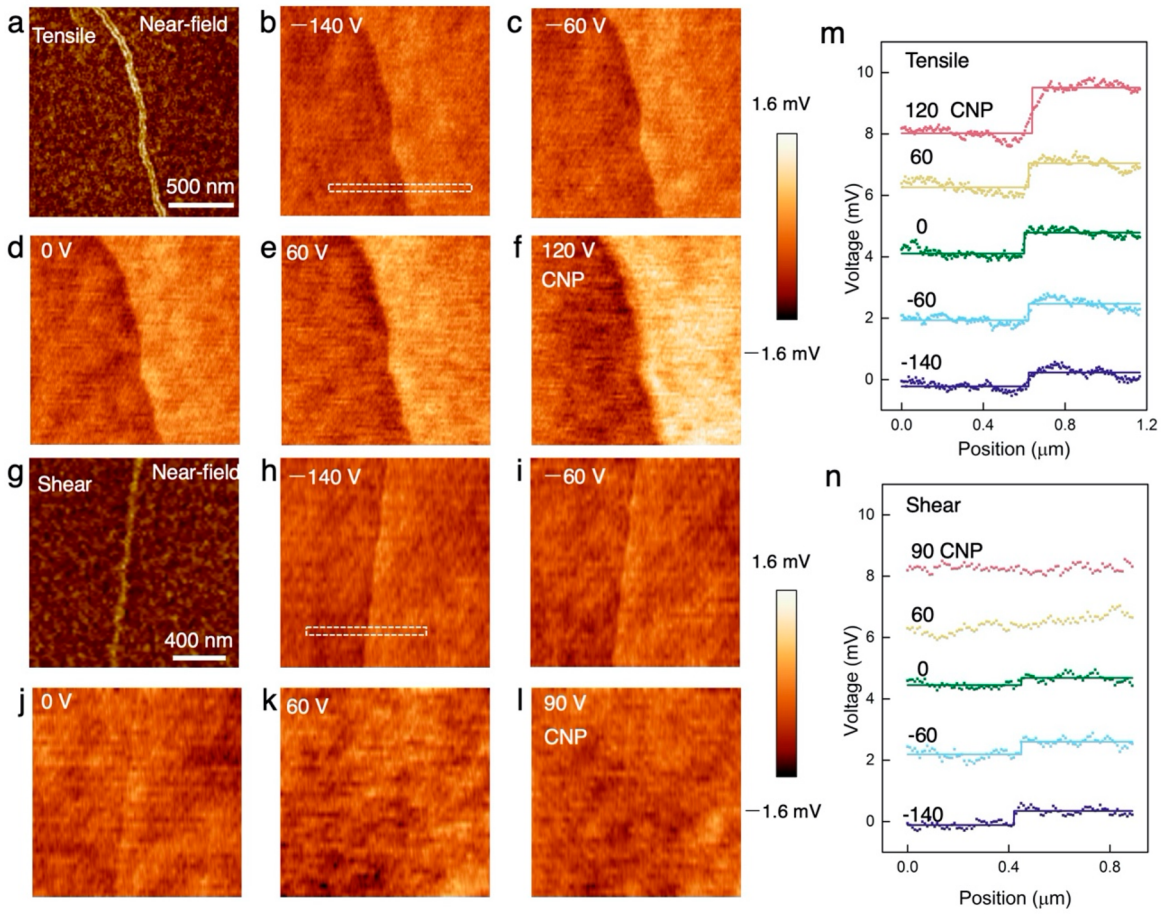

Figure 3. Gate-dependent transport across tensile and shear domain walls. (a) The near-field infrared image of a tensile domain wall in bilayer graphene. (b–f) Voltage images of the tensile domain wall at gate voltage from −140 to 120 V (CNP). The largest voltage drop appears at the CNP and decreases monotonically with increasing carrier density. (g) The near-field infrared image of a shear-type domain wall in bilayer graphene. (h,i) Voltage images of the shear domain wall at gate voltage from −140 to 90 V (CNP). The voltage drop is almost zero across the shear domain wall at the CNP and increases gradually as the carrier density increases. (m,n) Line profiles of the voltage across tensile and shear domain walls at various gate voltages. The line profiles are averaged along the domain wall over the area within the white dashed lines in (b) (tensile) and (h) (shear) to increase signal-to-noise ratio.

■ RESULTS AND DISCUSSION

We first employ near-field infrared nanoscopy to locate the domain walls in the exfoliated bilayer graphene flakes, which are invisible in topography images. Figure 1c displays the infrared nanoimaging technique which is based on a tapping mode atomic force microscopy (AFM) and coupled an infrared light onto the tip apex.[29,30] It can visualize the domain walls in bilayer graphene due to their interaction with graphene plasmons excited by the AFM metallic tip (see Methods for details). In addition, we can also identity the types of the domain walls due to the distinct features of the tensile and shear domain wall in the near-field infrared images.[11] Figure 1d,e shows the AFM topography image and near-field infrared image of a bilayer graphene flake with the domain walls inside. The topography image (Figure 1d) is almost featureless. Yet the near-field infrared image (Figure 1e) shows obviously bright lines in a homogeneous background. These bright lines are domain walls in bilayer graphene. There are two domain walls which are close to each other in the left part and then separate in the right part as shown in Figure 1e. The lower right domain wall segment shows a double-line feature, indicating it is a tensile-like domain wall while the upper segment shows a single-line feature, indicating it is a shear-like domain wall.

After locating and identifying the domain walls, we fabricate the bilayer graphene which is on SiO_2(285 nm)/Si substrate into a field-effect transistor (FET). The source and drain contact electrodes are evaporated by using shadow masks to avoid contamination on the graphene surface from nanofabrication. Figure 2a shows the experimental scheme used to map the voltage distribution of the bilayer graphene device with domain walls. The AFM is working under contact mode. A bias voltage is applied between the source and drain electrodes to generate current flow through the bilayer graphene channel. A back-gate voltage is applied between the Si substrate and the source electrode to change the carrier concentration in bilayer graphene. By using the metallic AFM tip as a local scanning voltage probe, we record the voltage distribution of the whole device with resolution limited by the radius of the tip apex (~25 nm) (see Methods for details). The voltage distribution of the bilayer graphene without domain walls exhibits linear slope along the average current direction (Figure S1 in Supporting Information). To focus on the voltage variation induced by the domain wall, we subtracted the linear voltage drop. An extra voltage drop at the domain

https://dx.doi.org/10.1021/acs.nanolett.0c01911
Nano Lett. 2020, 20, 5936−5942

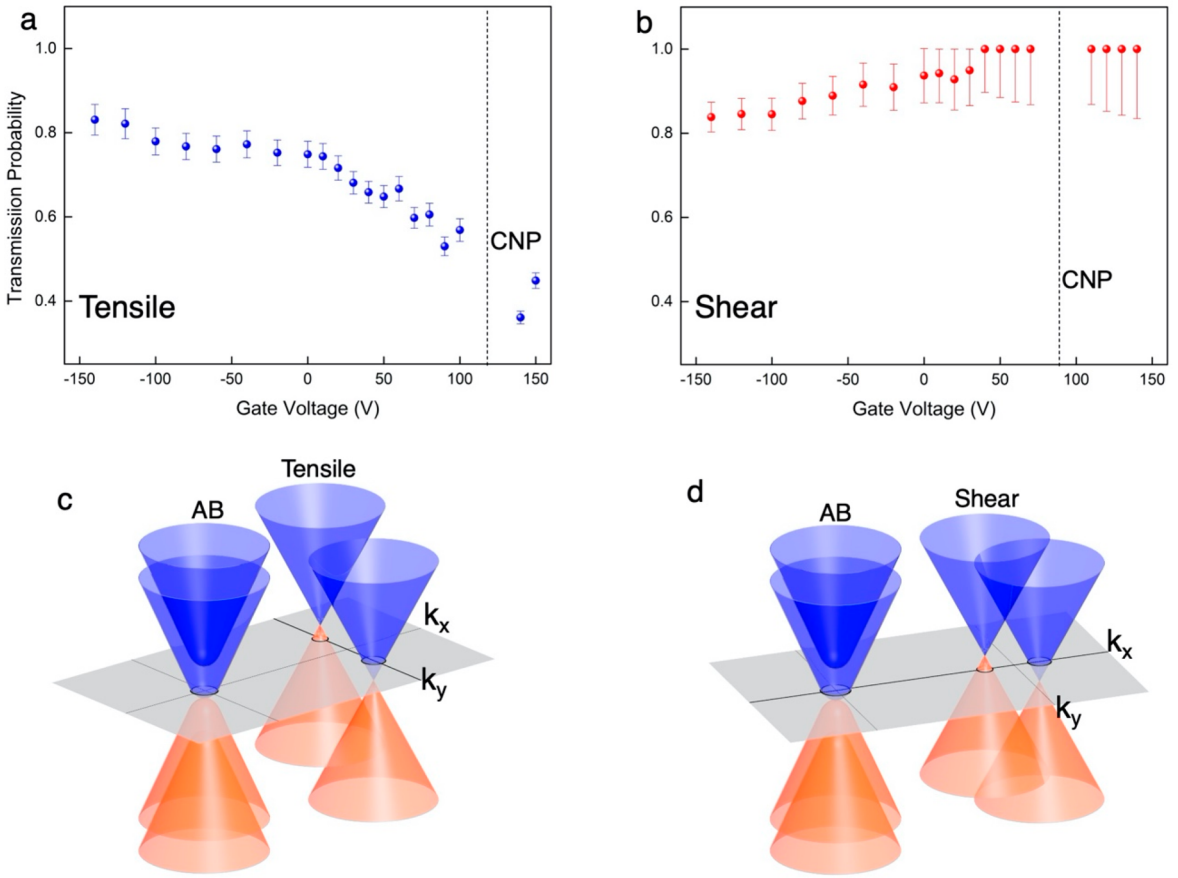

Figure 4. Gate-dependent transmission probability of tensile and shear domain. (a,b) The transmission probability as a function of the gate voltage at tensile and shear domain wall, respectively. The transmission probability across the tensile domain wall is relatively low at the CNP and increases with carrier doping. The transmission probability across the shear domain wall remains rather high over the whole doping range. (c) The schematic of the energy band structures of AB-stacked bilayer graphene and the tensile-type domain wall. k_x and k_y represent the longitudinal and transverse electron momentum that are perpendicular and parallel to the domain wall, respectively. At the tensile domain wall, the Fermi circles of the two graphene layers split along the k_y direction and no electron states with conserved transverse momentum (k_y) exist close to the CNP. (d) The schematic of the energy band structures of AB-stacked bilayer graphene and the shear domain wall. At the shear domain wall, the split is along the k_x direction, so electron states with conserved transverse momentum (k_y) always exist at different energy levels.

wall region is clearly observed, which is shown in Figure 2b. This demonstrates that the modification of the atomic structure at the domain wall indeed causes additional electron scattering. In addition, we found the magnitude of the extra voltage drop at the tensile domain wall is stronger than that at the shear domain wall. To quantitatively compare the voltage drops, we extract the line profiles across the tensile and shear domain walls and displayed them in Figure 2c. The profiles are averaged along the domain walls to increase the signal-to-noise ratio. The voltage drops at the tensile and shear domain walls are 0.99 and 0.30 mV, respectively. We estimated the extra resistance induced by the domain wall through the equation $\Delta V = jR_{DW}$, where ΔV is the extra voltage drop at the domain wall, j is the current density and R_{DW} is the extra resistance of the domain wall.[31] The calculated resistances of tensile and shear domain walls are ~12.6 Ω μm and ~3.8 Ω μm, respectively. Note that the presence of domain walls may alter the current density distribution. The domain wall resistance is much smaller compared to the channel resistance and therefore can be regarded as small local perturbation to the current density distribution. We can use the averaged global current density for estimation of the domain wall resistance here. This is also demonstrated in the numerical simulation of the potential map and current density distribution (see Figure S2 in Supporting Information for details).

It is also seen that at the two-domain wall (two-DW) area, the voltage drop looks even slightly weaker than the single tensile domain wall. We attribute this to the fact that both domain walls here are close to shear type. In this two-DW area, the left domain wall segment is still close to a shear type rather than tensile type because its direction is only slightly away from the shear domain wall segment on the top; while the right domain wall segment is also closer to a shear type since its direction is changed by roughly 90° compared to the tensile domain wall segment on the right. If we assume the voltage drop of the two-DW is equal to the sum of each single domain wall, then it is reasonable that the voltage drop across the two shear domain walls (close to shear type) is slightly smaller than the voltage drop across a tensile domain wall.

To further explore the electrical properties of different types of domain walls, we investigated gate-dependent voltage drops across the tensile and shear domain walls. We applied a constant bias voltage to the bilayer graphene transistor and mapped the voltage distribution at various back-gate voltages. Since the contact resistance between the source/drain electrode and the bilayer graphene is affected by the doping of graphene, we normalized the voltage maps at each back-gate

https://dx.doi.org/10.1021/acs.nanolett.0c01911
Nano Lett. 2020, 20, 5936−5942

voltage by keeping the total voltage drop across the bilayer graphene sample a constant. Figure 3a displays the near-field infrared image of a tensile domain wall (double-line feature). Figure 3b–f shows the normalized voltage maps from −140 to 120 V gate voltages (linear voltage drop is subtracted). The bias gradient is ∼65 mV/μm. From the transfer curve of the bilayer graphene transistor (Figure S3 in Supporting Information), we determined that the charge neutrality point (CNP) is at ∼120 V gate voltage. At −140 V gate voltage, the voltage drop at tensile domain wall is ∼0.58 mV. As the carrier density is decreased by electrostatic gating, the voltage drop of the tensile domain wall increases monotonically. The strongest voltage drop of the tensile domain wall appears at CNP, which is ∼1.8 mV (Figure 3f). Figure 3m shows the line profiles of the voltage across the tensile domain wall averaged in the white dashed area at various gate voltages. The dotted curves are extracted from the experimental data and the solid curves are the fitting voltage steps.

In marked comparison, the shear domain wall exhibits distinctly different gate-dependent transport behavior. Figure 3g shows the near-field infrared image of a shear domain wall (single-line feature). The voltage maps of the shear domain wall at different gate voltages are displayed in Figure 3h–l (linear voltage drop is subtracted). The applied bias gradient is ∼65 mV/μm. At −140 V gate voltage, the voltage drop is ∼0.58 mV. In contrast to the tensile domain wall, the voltage drop at the shear domain wall slightly decreases as carrier density decreases. At CNP (90 V), the map does not show apparent voltage discontinuity at the domain wall region. Figure 3n displays the line profiles of the voltage across the shear domain wall at various gate voltages. The different gate-dependent trend of the voltage drop at tensile (Figure 3m) and shear (Figure 3n) domain walls demonstrates that the electronic transport through the domain walls in bilayer graphene strongly depends on their atomic structures.

Next we estimate the electron transmission probability across the domain wall as a function of the gate voltage from the SVM measurements. The domain wall acts as a scattering source in the bilayer graphene channel and gives rise to additional resistance in series with the channel resistance. The transmission probability T_{DW} across the domain wall thus is closely associated with the additional resistance or voltage drop it induces. For a conducting channel with mean free path L_m, the transmission probability across a channel length L is $T = L_m/(L + L_m)$. Under given bias gradient F, the additional voltage drop ΔV at the domain wall can be converted into an effective channel length of $L_{eff} = \Delta V/F$ and the transmission probability across the domain wall can be described by

$$T_{DW} = \frac{L_m}{L_{eff} + L_m}$$

$L_m = \sigma\hbar\sqrt{\pi}/(e^2\sqrt{n})$ is the electron mean free path of the bilayer graphene, where σ is the conductivity, n is the carrier concentration, $\hbar$ is the reduced Plank constant, and e is the electron charge. Under given F, the transmission across the domain wall is related to the voltage drop ΔV as well as the electron mean free path L_m of the bilayer graphene device. The value of L_m as a function of the applied gate voltage is shown in Figure S4 in Supporting Information. In Figure 4a,b, we plotted the calculated transmission probability across the tensile and the shear domain walls at different back-gate voltages. The uncertainty of the measured voltage by SVM δ_V ∼ ±150 μV is determined by the instrument accuracy of the voltage meter at room temperature. The error bar for the transmission probability δ_T is related to δ_V as $\delta_T = \frac{-\delta_V L_m F}{(L_m F + \Delta V)^2}$. Because of the existence of electron and hole puddles at CNP and the associated uncertainty in estimating L_m, we calculated the electron transmission probability only away from the CNP. The transmission through the tensile domain wall shows an obvious gate-dependent behavior with a gradual increase as the carrier density increases under the applied gate voltage range (from 120 V (CNP) to −140 V). The shear domain wall remains highly transparent in the whole applied gate voltage range and has a transmission probability close to 1 near CNP.

Domain-wall soliton-dependent carrier transport in bilayer graphene has been predicted by theory.[28] Briefly, different atomic configurations inside the domain walls lead to different local electronic band structures at the domain wall, which can scatter incident electrons differently. For electrons to pass through the domain wall elastically, the electron energy and the transverse momentum have to be conserved. In an adiabatic picture, the domain wall barriers can be either highly transparent or insulating depending on whether the domain walls host continuous states that always conserve the energy and transverse momentum as the incident electrons. Figure 4c,d displays the schematics of the band structures of AB-stacked bilayer graphene, the tensile (corresponding to zigzag SP type in the theoretical work) and the shear (armchair SP type) domain wall. k_x and k_y represent the longitudinal and transverse electron momentum that are perpendicular and parallel to the domain wall directions, respectively. At the tensile domain wall, the Fermi circles split along the k_y direction (Figure 4c), which causes the tensile domain wall to be highly reflective for low-energy electrons because no electron states with conserved transverse momentum and energy exist in the domain wall. At higher electron energy, the transmission probability increases due to the finite phase space of the electronic states with conserved energy and momentum. In contrast, at the shear domain wall, the Fermi circles split along the k_x direction (Figure 4d). Therefore, the shear domain wall always hosts states for electrons to pass through elastically and will be highly transparent for all gate voltages, which is clearly observed in our transport measurement. Our data on soliton-dependent electron transmission across the domain walls agree qualitatively with this theoretical picture, except that the transmission probability across the tensile domain at the CNP remains finite. This might be due to the presence of electron and hole puddles in our experimental devices, or due to the rather narrow domain wall which is not fully captured by the adiabatic approximation.

CONCLUSION

In conclusion, we have experimentally visualized the voltage drop at individual domain walls in bilayer graphene by directly imaging the voltage distribution of the bilayer graphene FET devices. We correlate electronic transport across the domain walls with their local structures characterized by the infrared nanoscopy. Two distinct transport behaviors at the tensile- and shear-type domain walls are unambiguously observed, that is, the tensile domain wall has an energy-dependent electron transmission while the shear domain wall keeps high transmission at all measured energy level. Our results suggest that the local atomic structures of the domain walls could determine their electrical properties and lead to different

https://dx.doi.org/10.1021/acs.nanolett.0c01911
Nano Lett. 2020, 20, 5936−5942

transport behaviors. Combining our previous work on domain wall manipulation,[14] we anticipate the soliton-dependent transport across bilayer graphene domain walls could provide a valuable way to develop novel nanoelectronic devices based on such one-dimensional solitons.

METHODS

Samples and Devices Preparation. Bilayer graphene samples were mechanically exfoliated from graphite onto SiO_2(285 nm)/Si substrate. Electrical contacts of Cr/Au (5/50 nm) for source and drain are fabricated by stencil mask evaporation. The reason that we choose Si/SiO_2 substrate is that the domain walls can be easily moved around on hexagonal boron nitride (h-BN) substrate during SVM measurements.

Infrared Nanoimaging of Domain Walls. The infrared nanoimaging technique is based on a tapping mode AFM (Model Innova from Bruker). We focus an infrared light beam (λ = 10.6 μm) onto the apex of a conductive AFM tip. The enhanced optical field at the tip apex interacts with graphene underneath the tip and is scattered by the tip, carrying the local optical information on the sample. An MCT (HgCdTe) detector is used to collect the backscattered light in the far field. The metallic tip is modulated at a frequency $\Omega \sim 220$ kHz with an amplitude of ~60 nm. The near-field signal is demodulated at 3Ω by a lock-in amplifier (Zurich Instruments HF2LI) to suppress the background signal. Near-field images are recorded simultaneously with the topography information during the measurements.

Scanning Voltage Microscope Measurements. SVM measurements are based on a contact-mode AFM (Model Innova from Bruker) and performed under ambient conditions. A Keithley 2400 source meter is used to apply the bias between the two electrodes and also measure the generated current. Another Keithley 2400 source meter is used to apply the back-gate voltage between the highly doped silicon layer and the source electrode. The conductive AFM tip acted as a scanning probe, which recorded the potential maps of the devices simultaneously with the topography. The voltage meter recording the potential between the AFM tip and source channel has an impedance (2 GΩ) much larger than the tip−sample contact resistance (~kΩ). Therefore, the presence of the metallic tip does not alter the voltage distribution of the device. The uncertainty of the measured voltage ~±150 μV is determined by the instrument accuracy of the voltage meter at room temperature.

With the gate-dependent voltage maps for a measured region and recorded currents, we can determine the channel resistance (voltage drop divided by current normalized by the dimension) at different gate voltages. The dependence of channel resistance on gate voltage is summarized as a transfer curve of the device.

The SVM measurements shown in Figure 2b and Figure 3 are performed on a single bilayer graphene device. The dimension of the whole device is about 20 μm wide by 60 μm long. There are two domain walls in the whole device. One domain wall contains a tensile type segment (Figure 3a), and the other one contains a shear type segment (Figure 3g). The two domain walls go through the entire current channel. The current density is defined as a global averaged current density, assuming that the domain walls have a small effect on the large sample. The two sets of gate-dependent SVM measurements for the tensile and shear domain wall segments are done separately.

ASSOCIATED CONTENT

Supporting Information

The Supporting Information is available free of charge at https://pubs.acs.org/doi/10.1021/acs.nanolett.0c01911.

(1) Linear voltage drop of the bilayer graphene device, (2) numerical simulation of potential map and current density distribution, (3) transfer curves of the bilayer graphene devices, (4) mean free path L_m as a function of the gate voltages (PDF)

AUTHOR INFORMATION

Corresponding Author

Feng Wang − *Department of Physics, University of California at Berkeley, Berkeley, California 94720, United States; Materials Science Division, Lawrence Berkeley National Laboratory, Berkeley, California 94720, United States; Kavli Energy NanoSciences Institute at the University of California, Berkeley and the Lawrence Berkeley National Laboratory, Berkeley, California 94720, United States*; Email: fengwang76@berkeley.edu

Authors

Lili Jiang − *Department of Physics, University of California at Berkeley, Berkeley, California 94720, United States;* orcid.org/0000-0002-6930-4323

Sheng Wang − *Department of Physics, University of California at Berkeley, Berkeley, California 94720, United States; Materials Science Division, Lawrence Berkeley National Laboratory, Berkeley, California 94720, United States;* orcid.org/0000-0001-7923-478X

Sihan Zhao − *Department of Physics, University of California at Berkeley, Berkeley, California 94720, United States;* orcid.org/0000-0003-2162-734X

Michael Crommie − *Department of Physics, University of California at Berkeley, Berkeley, California 94720, United States; Materials Science Division, Lawrence Berkeley National Laboratory, Berkeley, California 94720, United States; Kavli Energy NanoSciences Institute at the University of California, Berkeley and the Lawrence Berkeley National Laboratory, Berkeley, California 94720, United States;* orcid.org/0000-0001-8246-3444

Complete contact information is available at: https://pubs.acs.org/10.1021/acs.nanolett.0c01911

Author Contributions

‖L.J. and S.W. contributed equally to this work.

Author Contributions

F.W. and L.J. conceived the project; L.J. and S.W. performed the SVM measurement; S.W. designed and built the circuits for AFM-based SVM; L.J. prepared the samples and performed the near-field IR measurements; L.J. and S.Z. made the FET devices; S.W. performed the numerical simulation. L.J., S.W. M.C. and F.W. analyzed the data. All authors discussed the results and contributed to writing the manuscript.

Notes

The authors declare no competing financial interest.

https://dx.doi.org/10.1021/acs.nanolett.0c01911
Nano Lett. 2020, 20, 5936−5942

■ ACKNOWLEDGMENTS

We acknowledge helpful discussions with Prof. Jeil Jung and Dr. Nicolas Leconte. We thank Prof. J. Velasco Jr. and Arturo Quezada for their help on sample preparation. This work was mainly supported by the Director, Office of Science, Office of Basic Energy Sciences, Materials Sciences and Engineering Division of the U.S. Department of Energy under Contract No. DE-AC02-05-CH11231 (sp2-Bonded Materials Program KC2207). The near-field measurement was supported by the NSF award 1808635. The FET device fabrication was supported by the Office of Naval Research (MURI award N00014-16-1-2921).

■ REFERENCES

(1) Ju, L.; Shi, Z.; Nair, N.; Lv, Y.; Jin, C.; Velasco, J., Jr; Ojeda-Aristizabal, C.; Bechtel, H. A.; Martin, M. C.; Zettl, A.; Analytis, J.; Wang, F. Topological valley transport at bilayer graphene domain walls. *Nature* **2015**, *520*, 650.

(2) Zhang, F.; Jung, J.; Fiete, G. A.; Niu, Q. A.; MacDonald, A. H. Spontaneous Quantum Hall States in Chirally Stacked Few-Layer Graphene Systems. *Phys. Rev. Lett.* **2011**, *106*, 106.

(3) Martin, I.; Blanter, Y. M.; Morpurgo, A. F. Topological Confinement in Bilayer Graphene. *Phys. Rev. Lett.* **2008**, *100*, 036804.

(4) Vaezi, A.; Liang, Y.; Ngai, D. H.; Yang, L.; Kim, E.-A. Topological Edge States at a Tilt Boundary in Gated Multilayer Graphene. *Phys. Rev. X* **2013**, *3*, 021018.

(5) Zhang, F.; MacDonald, A. H.; Mele, E. J. Valley Chern numbers and boundary modes in gapped bilayer graphene. *Proc. Natl. Acad. Sci. U. S. A.* **2013**, *110*, 10546.

(6) Semenoff, G. W.; Semenoff, V.; Zhou, F. Domain Walls in Gapped Graphene. *Phys. Rev. Lett.* **2008**, *101*, 087204.

(7) Yin, L.-J.; Jiang, H.; Qiao, J.-B.; He, L. Direct imaging of topological edge states at a bilayer graphene domain wall. *Nat. Commun.* **2016**, *7*, 11760.

(8) Li, J.; Wang, K.; McFaul, K. J.; Zern, Z.; Ren, Y.; Watanabe, K.; Taniguchi, T.; Qiao, Z.; Zhu, J. Gate-controlled topological conducting channels in bilayer graphene. *Nat. Nanotechnol.* **2016**, *11*, 1060.

(9) Li, J.; Zhang, R.-X.; Yin, Z.; Zhang, J.; Watanabe, K.; Taniguchi, T.; Liu, C.; Zhu, J. A valley valve and electron beam splitter. *Science* **2018**, *362*, 1149.

(10) Cheng, S.-g.; Liu, H.; Jiang, H.; Sun, Q.-F.; Xie, X. C. Manipulation and Characterization of the Valley-Polarized Topological Kink States in Graphene-Based Interferometers. *Phys. Rev. Lett.* **2018**, *121*, 156801.

(11) Jiang, L.; Shi, Z.; Zeng, B.; Wang, S.; Kang, J.-H.; Joshi, T.; Jin, C.; Ju, L.; Kim, J.; Lyu, T.; Shen, Y.-R.; Crommie, M.; Gao, H.-J.; Wang, F. Soliton-dependent plasmon reflection at bilayer graphene domain walls. *Nat. Mater.* **2016**, *15*, 840.

(12) Sunku, S. S.; Ni, G. X.; Jiang, B. Y.; Yoo, H.; Sternbach, A.; McLeod, A. S.; Stauber, T.; Xiong, L.; Taniguchi, T.; Watanabe, K.; Kim, P.; Fogler, M. M.; Basov, D. N. Photonic crystals for nano-light in moiré graphene superlattices. *Science* **2018**, *362*, 1153.

(13) Butz, B.; Dolle, C.; Niekiel, F.; Weber, K.; Waldmann, D.; Weber, H. B.; Meyer, B.; Spiecker, E. Dislocations in bilayer graphene. *Nature* **2014**, *505*, 533.

(14) Jiang, L.; Wang, S.; Shi, Z.; Jin, C.; Utama, M. I. B.; Zhao, S.; Shen, Y.-R.; Gao, H.-J.; Zhang, G.; Wang, F. Manipulation of domain-wall solitons in bi- and trilayer graphene. *Nat. Nanotechnol.* **2018**, *13*, 204.

(15) Schweizer, P.; Dolle, C.; Spiecker, E. In situ manipulation and switching of dislocations in bilayer graphene. *Sci. Adv.* **2018**, *4*, eaat4712.

(16) Lin, J.; Fang, W.; Zhou, W.; Lupini, A. R.; Idrobo, J. C.; Kong, J.; Pennycook, S. J.; Pantelides, S. T. AC/AB Stacking Boundaries in Bilayer Graphene. *Nano Lett.* **2013**, *13*, 3262.

(17) Alden, J. S.; Tsen, A. W.; Huang, P. Y.; Hovden, R.; Brown, L.; Park, J.; Muller, D. A.; McEuen, P. L. Strain solitons and topological defects in bilayer graphene. *Proc. Natl. Acad. Sci. U. S. A.* **2013**, *110*, 11256.

(18) Li, G.; Luican, A.; Lopes dos Santos, J. M. B.; Castro Neto, A. H.; Reina, A.; Kong, J.; Andrei, E. Y. Observation of Van Hove singularities in twisted graphene layers. *Nat. Phys.* **2010**, *6*, 109.

(19) Cao, Y.; Fatemi, V.; Demir, A.; Fang, S.; Tomarken, S. L.; Luo, J. Y.; Sanchez-Yamagishi, J. D.; Watanabe, K.; Taniguchi, T.; Kaxiras, E.; Ashoori, R. C.; Jarillo-Herrero, P. Correlated insulator behaviour at half-filling in magic-angle graphene superlattices. *Nature* **2018**, *556*, 80.

(20) Cao, Y.; Fatemi, V.; Fang, S.; Watanabe, K.; Taniguchi, T.; Kaxiras, E.; Jarillo-Herrero, P. Unconventional superconductivity in magic-angle graphene superlattices. *Nature* **2018**, *556*, 43.

(21) Rickhaus, P.; Wallbank, J.; Slizovskiy, S.; Pisoni, R.; Overweg, H.; Lee, Y.; Eich, M.; Liu, M.-H.; Watanabe, K.; Taniguchi, T.; Ihn, T.; Ensslin, K. Transport Through a Network of Topological Channels in Twisted Bilayer Graphene. *Nano Lett.* **2018**, *18*, 6725.

(22) Yoo, H.; Engelke, R.; Carr, S.; Fang, S.; Zhang, K.; Cazeaux, P.; Sung, S. H.; Hovden, R.; Tsen, A. W.; Taniguchi, T.; Watanabe, K.; Yi, G.-C.; Kim, M.; Luskin, M.; Tadmor, E. B.; Kim, E.; Kaxiras, P. Atomic and electronic reconstruction at the van der Waals interface in twisted bilayer graphene. *Nat. Mater.* **2019**, *18*, 448.

(23) Bistritzer, R.; MacDonald, A. H. Moiré bands in twisted double-layer graphene. *Proc. Natl. Acad. Sci. U. S. A.* **2011**, *108*, 12233.

(24) Po, H. C.; Zou, L.; Vishwanath, A.; Senthil, T. Origin of Mott Insulating Behavior and Superconductivity in Twisted Bilayer Graphene. *Phys. Rev. X* **2018**, *8*, 031089.

(25) Tarnopolsky, G.; Kruchkov, A. J.; Vishwanath, A. Origin of Magic Angles in Twisted Bilayer Graphene. *Phys. Rev. Lett.* **2019**, *122*, 106405.

(26) Huang, S.; Kim, K.; Efimkin, D. K.; Lovorn, T.; Taniguchi, T.; Watanabe, K.; MacDonald, A. H.; Tutuc, E.; LeRoy, B. J. Topologically Protected Helical States in Minimally Twisted Bilayer Graphene. *Phys. Rev. Lett.* **2018**, *121*, 037702.

(27) Yankowitz, M.; Chen, S.; Polshyn, H.; Zhang, Y.; Watanabe, K.; Taniguchi, T.; Graf, D.; Young, A. F.; Dean, C. R. Tuning superconductivity in twisted bilayer graphene. *Science* **2019**, *363*, 1059.

(28) Koshino, M. Electronic transmission through AB-BA domain boundary in bilayer graphene. *Phys. Rev. B: Condens. Matter Mater. Phys.* **2013**, *88*, 115409.

(29) Fei, Z.; Rodin, A. S.; Andreev, G. O.; Bao, W.; McLeod, A. S.; Wagner, M.; Zhang, L. M.; Zhao, Z.; Thiemens, M.; Dominguez, G.; Fogler, M. M.; Neto, A. H. C.; Lau, C. N.; Keilmann, F.; Basov, D. N. Gate-tuning of graphene plasmons revealed by infrared nano-imaging. *Nature* **2012**, *487*, 82.

(30) Chen, J.; Badioli, M.; Alonso-Gonzalez, P.; Thongrattanasiri, S.; Huth, F.; Osmond, J.; Spasenovic, M.; Centeno, A.; Pesquera, A.; Godignon, P.; Zurutuza Elorza, A.; Camara, N.; de Abajo, F. J. G.; Hillenbrand, R.; Koppens, F. H. L. Optical nano-imaging of gate-tunable graphene plasmons. *Nature* **2012**, *487*, 77.

(31) Ji, S.-H.; Hannon, J. B.; Tromp, R. M.; Perebeinos, V.; Tersoff, J.; Ross, F. M. Atomic-scale transport in epitaxial graphene. *Nat. Mater.* **2012**, *11*, 114.

https://dx.doi.org/10.1021/acs.nanolett.0c01911
Nano Lett. 2020, 20, 5936−5942